Inhibiting ACSL1 related ferroptosis restrains MHV-A59 infection

Huawei Xia[1], Zeming Zhang[1], Fuping You[1, *].

[1]Department of Systems Biomedicine, Institute of Systems Biomedicine, School of Basic Medical Sciences, Peking University Health Science Center, Beijing, China.

[*]Corresponding author

Address correspondence and reprint requests to Dr. Fuping You, Institute of Systems Biomedicine, School of Basic Medical Sciences, Peking University Health Science Center, Beijing 100191, China. E-mail address: fupingyou@hsc.pku.edu.cn

Abstract

Murine hepatitis virus strain A59 (MHV-A59) belongs to the β-coronavirus and is considered as a representative model for studying coronavirus infection. MHV-A59 was shown to induce pyroptosis, apoptosis and necroptosis of infected cells, especially the murine macrophages. However, whether ferroptosis, a recently identified form of lytic cell death, was involved in the pathogenicity of MHV-A59, is unknown. Here, we demonstrate inhibiting ferroptosis suppresses MHV-A59 infection. MHV-A59 infection upregulates the

expression of *Acsl1*, a novel ferroptosis inducer. MHV-A59 upregulates *Acsl1* expression depending on the NF-kB activation, which is TLR4-independent. Ferroptosis inhibitor inhibits viral propagation, inflammatory cytokines release and MHV-A59 infection induced cell syncytia formation. ACSL1 inhibitor Triacsin C suppresses MHV-A59 infection induced syncytia formation and viral propagation. *In vivo* administration of liproxstatin-1 ameliorates lung inflammation and tissue injuries caused by MHV-A59 infection. Collectively, these results indicate that ferroptosis inhibition protects hosts from MHV-A59 infection. Targeting ferroptosis may serves as a potential treatment approach for dealing with hyper-inflammation induced by coronavirus infection.

Introduction

SARS-CoV-2, the causative agent of the coronavirus disease 2019 (COVID-19), has resulted in more than 4 million deaths worldwide. Thus, studying coronavirus and interaction between coronavirus and hosts can help understand the mechanism within the infection process and provide new approaches for clinical treatment. Murine hepatitis virus strain A59 (MHV-A59) is a well-studied coronavirus infection model (1). It has been validated that lung infection of MHV-A59 was sufficient to cause pneumonia and severe lung injuries (2, 3). Expression of inflammatory cytokines such as *Cxcl10*, *Ifng* and *Il6* were potently elevated in the lungs of infected mice. Mice with intranasal inoculation of

MHV-A59 exhibited typical acute inflammatory response with large areas of hemorrhages. Our previous study also showed that intranasal MHV-A59 infection mouse model mimicked the hyper-inflammation induced by SARS-CoV-2 infection (4), further suggesting that intranasal inoculation with MHV-A59 can serve as a surrogate mouse model for studying COVID-19.

Ferroptosis is a newly identified iron-dependent necrotic cell death, mainly raised by the accumulation of lipid reactive oxygen species (ROS), resulting in excessive lipid peroxidation and subsequent cell membrane damage (5, 6, 7). Ferroptosis can be divided into two types, namely canonical and non-canonical types, according to their dependency on the involvement of GPX4. In the canonical ferroptosis, inactivation or depletion of GPX4 leads to the lack of glutathione (GSH) and lipid ROS overload, making the cell membrane vulnerable to lipid peroxidation (8). The non-canonical ferroptosis is characterized by the inactivation of ferroptosis suppressor protein 1 (FSP1), which maintains the active pool of radical-trapping antioxidant coenzyme Q10 (9, 10). In addition, cystine/glutamate transporter (xCT), encoded by *Slc7a11*, transfers cystine, the central material for generating GSH, into the cytosol to prevent ROS overload induced cell damage (11). Peroxidation of phospholipid species acts as the execution stage of ferroptosis. At the execution stage, for example, polyunsaturated fatty acids (PUFAs) can be esterified by acyl-CoA synthetase long-chain family member 4 (ACSL4), which occurs at the cell membrane, leading to the cell membrane rupture (12, 13, 14). Recently, acyl-CoA synthetase long-chain family member 1 (ACSL1) was uncovered as a ferroptosis promoter (15). ACSL1 promoted α-eleostearic acid (αESA) triggered

ferroptosis. However, the αESA triggered ACSL1 dependent ferroptosis was distinct from the ferroptosis induced by the canonical ferroptosis inducers, including the GPX4 inhibitor ML160 and the FSP1 inhibitor iFSP1. ACSL1 has only been validated to participant in a murine breast cancer xenograft model (16). How ACSL1 involves in other biological processes is unknown.

Viral infection induces various kinds of programed cell death, including apoptosis, necroptosis and pyroptosis (17). For the β-coronavirus infection, cells were reported to undergo PANoptosis, which consisted of Pyroptosis, Apoptosis and Necroptosis (18, 19). Previous studies have shown that SARS-CoV-2 can induce these three kinds of programed cell death in susceptible epithelial cells and immune cells (20, 21, 22). As for ferroptosis, whose morphological and biochemical features are distinct from PANoptosis, new castle virus (NDV) was the first virus to be discovered as ferroptosis inducer in tumor cells (23). NDV infection reduced the expression of *Slc7a11* and *Gpx4*, resulting in the ferroptosis of infected cells. Apart from NDV, so far, no other viruses were reported to induce ferroptosis of infected cells, although hepatitis B, hepatitis C, HIV-1 and human cytomegalovirus infection caused increased serum iron level (24, 25).

Ferroptosis has been linked with inflammation and immune responses. In innate immunity, GPX4 deficiency dampens cGAS-STING dependent innate immune signaling activation (26). Neutrophils from systemic lupus erythematosus (SLE) patients exhibit ferroptosis due to the transcriptional repression of *GPX4* (27). In adaptive immunity, GPX4 is essential for maintaining the metastasis of T_{FH} cells and promotes humoral immune responses (28). Ferroptosis of non-leukocytic cells often results in the release and

activation of different damage-associated molecular pattern (DAMP), triggering the inflammatory responses (29, 30). Because COVID-19 patients suffered from systemic hyper-inflammation, characterized by ROS elevation and cytokine storm, SARS-CoV-2 infection was predicted to involve ferroptosis (31, 32, 33). The prediction was also evidenced by the elevated serum iron load in COVID-19 patients and decreased *GPX4* expression in SARS-CoV-2 infected cells (34, 35, 36). Here we showed that MHV-A59 infection induced *Acsl1* expression and ferroptosis of murine macrophages. Inhibition of ACSL1 with Triacsin C and ferroptosis inhibitors protected cells from MHV-A59 infection. Intranasal inoculation of liproxstatin-1 ameliorated MHV-A59 infection induced hemorrhagic alterations and immune cells infiltration in lungs of infected mice. Our study provides evidence for targeting ferroptosis to deal with coronavirus infection.

Results

Ferroptosis inhibitors suppressed syncytia formation after MHV-A59 infection

Coronavirus infection results in typical cell-cell fusion named syncytia (37). Syncytia formation of SARS-CoV-2 or MHV-A59 infected cells mainly depends on the interaction between spike protein and receptors and indicates the viral abundance and cellular antiviral mechanism (38). Although certain cell types such as lung epithelial cells and

colorectal epithelial cells are susceptible to SARS-CoV-2, it has been reported that SARS-CoV-2 was able to infect macrophages (39, 40, 41). Both MHV-A59 and SARS-CoV-2 can infect murine macrophages. MHV-A59 infected murine bone marrow derived macrophages (BMDMs) and peritoneal macrophages (PMs) via the canonical receptor Ceacam1 (42), while Nrp1 mediated SARS-CoV-2 infection of murine macrophages and human olfactory epithelium (43, 44, 45). Given that coronavirus infection in macrophages promotes the inflammatory responses, which involves pro-inflammatory cell death programs, we intended to determine whether ferroptosis contributes to the pathogenicity of coronavirus. We first monitored cell morphology of both BMDM and PM after MHV-A59 infection for 24 hours. Cell-cell fusion resulted in multinucleated cell formation, followed by the appearance of squeezed out vacuole and subsequent cell death, which was ferroptosis-like (Video S1). It has been shown that syncytia were observed in tissues from deceased patients with pulmonary manifestations compared with those without pulmonary manifestations (38). We next used ferrostatin-1 (Fer-1), a ferroptosis inhibitor that functions via trapping radical, to check whether ferroptosis inhibition influenced MHV-A59 infection (46, 47). Syncytia formed by peritoneal macrophages was apparently inhibited by Fer-1 (Figure 1A and 1B). Besides, Fer-1 also protected cells from membrane damage (Figure 1C). In contrast, the caspase-3 inhibitor z-DEVD-FMK and caspase-1 inhibitor VX765 showed no obvious effect on cell membrane integrity maintenance, whereas the RIPK3 inhibitor GSK-872 exerted protective effects similar with Fer-1 (Figure 1D). Collectively, these results indicated that ferroptosis inhibition protected murine macrophages from MHV-A59 infection.

133

134 Ferroptosis inhibitors reduced viral load and inflammatory cytokine release after MHV-A59
135 infection

136

137 We next intended to find how ferroptosis inhibitors restrict MHV-A59 infection. We first
138 tested genomic RNA level of MHV-A59 after 2 hours of infection. Fer-1 administration had
139 minimal effects on invasion of MHV-A59 into macrophages (Figure S1). After excluding
140 the possibility that Fer-1 inhibited viral entry, we next wanted to know whether Fer-1
141 inhibited MHV-A59 propagation. Interestingly, quantitative PCR results showed that
142 intracellular MHV RNA level was identical or even slightly higher in cells treated with Fer-1
143 after infection (Figure 2A). However, via evaluating the viral titer in the cell culture
144 supernatant, we found that viral load was lower after Fer-1 treatment (Figure 2B). These
145 results suggested that ferroptosis inhibition affected viral propagation of MHV-A59.
146 Because ferroptosis often occurs along with inflammatory cytokine release (48), we
147 wanted to determine how ferroptosis inhibition influenced MHV-A59 induced inflammation.
148 Fer-1 treatment showed no significant effect on the expression of inflammatory cytokines
149 (*Il6*, and *Cxcl10*) and type I interferon (*Ifnb1*) (Figure 2C and 2D). However, Fer-1 treated
150 macrophages released lower level of IL-6 (Figure 2E). These data suggested that
151 ferroptosis inhibition reduced inflammatory cytokine release after MHV-A59 infection. LDH
152 release level has been used to evaluate cell viability in lytic cell death. We thus also
153 checked effects of Fer-1 on LDH release after MHV-A59 infection. As shown in Figure 2F,
154 less LDH was released from Fer-1 treated cells, indicating the higher viability of cells after

ferroptosis inhibition. Taken together, these data indicated that ferroptosis inhibition restricted propagation of MHV-A59 and inflammatory cytokine release induced by MHV-A59 infection.

Liproxstatin-1 ameliorated MHV-A59 infection induced inflammation and lung injury

We next checked the efficiency of ferroptosis inhibitors on inhibiting MHV-A59 lung infection. We selected C57BL/6 mice to carry out the viral infection experiments, because intranasal inoculation of MHV-A59 was reported to cause severe lung inflammation and tissue injury in this mouse strain. Liproxstatin-1 (Lip-1) functions as another radical-trapping ferroptosis inhibitor and has been selected as ferroptosis inhibitor in several mouse models (8, 27). We thus assessed the influences of Lip-1 treatment on MHV-A59 lung infection. Daily intranasal treatment of Lip-1 was carried out after MHV-A59 infection until day 10 post infection (Figure 3A). Comparison of pathologic alterations in lungs of mice between MHV-A59 infection alone group and infection together with Lip-1 treatment group showed that Lip-1 treated group exhibited less severe pneumonia, characterized by less hemorrhagic alterations and less immune cells infiltration (Figure 3B, 3C and 3D). However, such model applying low dose of MHV-A59 resulted in no significant difference in body weight changes between groups with or without Lip-1 treatment after MHV-A59 inoculation (Figure S2). Taken together, these data suggested that Lip-1 ameliorated inflammatory responses and tissue injury in lung after MHV-A59 infection.

177

178 MHV-A59 infection induced potent *Acsl1* expression

179

180 We next intended to investigate how MHV-A59 infection induced ferroptosis. Although
181 MHV-A59 infection was reported to induce enrichment of serum iron level and ROS
182 abundance elevation in infected mice, the executor of this process remained unclear,
183 especially in terms of ferroptosis. We infected murine BMDMs and performed bulk
184 RNA-seq to figure out the expression profile changes brought by MHV-A59 in innate
185 immune cells. MHV-A59 infection led to canonical inflammatory genes upregulation,
186 characterized by the elevated expression of genes responsible for inflammatory
187 responses (Figure 4A). Interestingly, compared with other members of acyl-CoA
188 synthetase long-chain family, we noticed that expression of the newly identified ferroptosis
189 executor ACSL1 was potently induced by MHV-A59 (Figure 4B and 4C). The upregulation
190 of *Acsl1* was further confirmed in the RNA-seq data of murine PMs infected with MHV-A59
191 (Figure 4D). We also noticed the elevated expression of ferroptosis biomarker *Ptgs2* after
192 MHV-A59 infection (49) (Figure 4E). We further checked the expression of *Acsl1* in
193 several cell lines, turning out that apparent upregulation of *Acsl1* only occurred in primary
194 macrophages (Figure 4F). In line with this, we failed to observe protective effects of
195 ferroptosis inhibition after MHV-A59 infection in RAW 264.7 cells, compared with that
196 observed in primary macrophages, suggesting that these protective effects may only exist
197 in primary macrophages (Figure S3). We thus reckoned that MHV-A59 induced
198 ferroptosis, which was dependent of the function of ACSL1. *Acsl1* was considered as an

199 indicator of severe sepsis in addition to *Acsl4* (50). Because TLR4 activation by ligands
200 such as LPS was one of the dominant causes for severe sepsis in bacterial infection and
201 TLR4 inhibition by TAK-242 alleviated fatal infection by MHV-A59 (51, 52, 4), we
202 reasoned that *Acsl1* upregulation may be the consequence of TLR4 signaling activation.
203 Results showed that TAK-242 treatment had no inhibitory effect on MHV infection
204 enhanced *Acsl1* expression (Figure 4G). Considering that NF-κB activation was
205 responsible for the explosive expression of various inflammatory genes and NF-κB
206 inhibition suppressed *Acsl1* expression in hepatocellular carcinoma cells (53), we checked
207 whether NF-κB inhibition attenuated *Acsl1* expression. As a result, the NF-κB inhibitor
208 JSH-23 suppressed MHV infection induced *Acsl1* upregulation (Figure 4H). Together,
209 these data suggested that MHV-A59 infection led to potent *Acsl1* upregulation in murine
210 macrophages.
211
212 Inhibiting acyl-CoA synthetase long-chain family members suppressed MHV-A59 infection
213
214 Base on the results above, we suspected that targeting ACSL1 may help eliminate
215 MHV-A59 infection. Two individual compound screening studies have found that Triacsin
216 C inhibited SARS-CoV-2 replication (54, 55), supporting our hypothesis. We first
217 determined the effects of ACSL1 inhibitor Triacsin C on MHV-A59 infection in murine
218 macrophages. Triacsin C treatment significantly suppressed MHV-A59 propagation in
219 both PMs and BMDMs (Figure 5A and 5B). In addition, Triacsin C also exerted little impact
220 on inflammatory cytokines expression after MHV infection, similar with ferroptosis

inhibitors (Figure 5C and 5D). Furthermore, Triacsin C reduced MHV-A59 induced syncytia formation (Figure 5E and 5F, see also Figure S4). These results suggested that ACSL1 inhibitor Triacsin C suppressed MHV-A59 infection.

Discussion

In this study, we found that ferroptosis inhibitors alleviated MHV-A59 infection induced inflammation, cell syncytia formation and prevented cell death. MHV-A59 triggered potent *Acsl1* expression in murine macrophages and acyl-CoA synthesis inhibitor Triacsin C efficiently suppressed MHV-A59 infection. Our findings provided evidence for targeting ferroptosis inhibition in treating coronavirus infection related diseases.

Ferroptosis has been linked with inflammatory responses. Ferroptosis inhibition was reported to protect hepatocytes from necrotic death and suppressed immune cells infiltration in mouse nonalcoholic steatohepatitis (NASH) (57). The pro-inflammatory ligand LPS induced lipid peroxidation and injury of myofibroblast, which were inhibited by Fer-1 (58). The pro-inflammatory effects of ferroptosis can be attributed to the functional alterations of cells undergoing ferroptosis. On one hand, for immune cells, ferroptosis usually functioned via regulating their traditional activity. For example, ferroptosis in T cells suppressed T cell expansion and prevented viral clearance (59). Ferroptosis was involved in Mycobacterium tuberculosis induced necrotic cell death of macrophages and

was inhibited by Fer-1 (60). On the other hand, ferroptosis in somatic cells can trigger immune cell infiltration, leading to inflammation. One example is that ferroptotic cells release HMGB1, a kind of damage-associated molecular pattern molecules (DAMPs), and mediates inflammation in macrophages (29). Given the facts above, we speculated that ferroptosis inhibition may contribute to inflammation suppression in excessive inflammation, especially in terms of coronavirus infection. SARS-CoV-2 infection can result in systemic hyper-inflammation in severe COVID-19 patients, which may be partially due to occurrence of ferroptosis. Several reviews mentioned about the possibility of ROS elimination for treatment of COVID-19. Although in one case, the application of N-acetylcysteine (NAC), a ferroptosis inhibitor that promotes glutathione supplementation, restored glutathione levels in the SARS-CoV-2 infected cells and markedly reduced C-reactive protein (CRP) level in a severe COVID-19 patient, another randomized clinical trial indicated that high dose of NAC brought little benefit to retarding the evolution of severe COVID-19 (61, 62, 63). However, our results here showed that ferroptosis inhibitor suppressed inflammatory cytokines release and MHV-A59 propagation in murine macrophages. In addition, we found that ferroptosis inhibition protected mice from MHV caused lung injury *in vivo*. Our findings broadened the application of ferroptosis inhibitors in treatments of inflammatory diseases, especially the hyper-inflammation status in coronavirus infection.

Ferroptosis is a kind of necrotic cell death characterized by the damages on cell membrane. Cell membrane rupture in lytic cell death can lead to the release of cellular components independent of canonical secretory systems, including LDH, which has been

reckoned as a marker for evaluating the cell viability in lytic cell death, and cytokines such as IL-1B, TNF-α, IL-6 and CXCL-10. Differed from necroptosis and pyroptosis, until now, cell membrane rupture in ferroptosis is considered as the result of a chemical process named phospholipid peroxidation, compared with MLKL-dependent or Gasdermins-dependent pore formation. Phospholipid peroxidation on cell membrane can be reversed by free radical elimination or radical-trapping by compounds such as Fer-1 and Lip-1. Our results showed that Fer-1 and Lip-1 addition reduced viral load of MHV in cell culture supernatant, whereas the cellular level of MHV RNA was not significantly affected. This may be attributed to the reduced cell membrane damage, which may help prevent the release of viral particles. However, former studies claimed that MHV release from infected cells was mainly through lysosomes, raising the importance of inhibiting lysosome-dependent egress path. We propose that inhibiting both ferroptosis and lysosome trafficking can provide great assistance on restricting coronavirus invasion and propagation. Besides, reduced inflammatory cytokines release owing to the protective effects of ferroptosis inhibitors on cell membrane can contribute to the limitation of inflammation. Taken together, these effects indicated that cell membrane protection brought by ferroptosis inhibition can be considered as a method to restrict coronavirus infection.

ACSL1 plays important roles in regulating fatty acid metabolism in adipose tissue, liver, heart and many other tissues and organs. In immune system, upregulated *Acsl1* expression promoted inflammatory phenotype of macrophages isolated from mouse models of type 1 diabetes (64). It is possible that high level of *Acsl1* expression induced by

coronavirus infection can directly enhance inflammatory phenotypes of infected macrophages via remodeling of lipid metabolism. Although inhibiting fatty acid synthesis was reported to block SARS-CoV-2 replication (65), it is still unclear how coronavirus infection alters the cellular lipid metabolism, especially the involvement of acyl-CoA synthetase long-chain family members. As a member of acyl-CoA synthetase long-chain family member,ACSL1 was recently identified to promote α-eleostearic acid triggered ferroptosis. However, the relationship between ferroptosis and inflammatory phenotypes in coronavirus infected macrophages is still elusive. Apart from macrophages, ACSL1 was also observed to be highly expressed in neutrophils in fatal sepsis (50). Our *in vivo* data revealed that ferroptosis inhibition protected mice from MHV infection,. The protective effects may be ACSL1-dependent. Taking the sepsis-like symptoms of COVID-19 patients into consideration, ACSL1 may serve as an intriguing therapeutic target to restrict cytokine storm in COVID-19.

Upregulation of *Acsl1* was reported to depended on Toll-like receptors and NF-κB. In our experiments, we evaluated the effects of TLR4 inhibitor TAK-242 and NF-κB inhibitor JSH-23 on expression of *Acsl1*. We observed that induction of *Acsl1* in MHV infected macrophages was NF-κB-dependent and TLR4-signaling-independent. Although our previous study indicated the importance of TLR4 signaling in restricting MHV infection, our results here showed that in macrophages, *Acsl1* upregulation required NF-κB but not TLR4 activation. Because Acsl1 expression also depends on TLR2 and TLR2 deficiency renders mice more protected from MHV infection (56, 66), we speculate that TLR2 signaling is responsible for MHV induced *Acsl1* expression and plays more important roles

than TLR4 signaling in mediating MHV infection. Different from SARS-CoV-2 infection, which was reported to downregulate *GPX4* expression, however, MHV infection resulted in no significant reduction of *Gpx4* expression, indicating distinct routines of ferroptosis occurrence between SARS-CoV-2 and MHV infection.

Triacsin C is a pan-acyl-CoA synthetase inhibitor which exerts inhibitory effects on ACSL1, ACSL3 and ACSL4. For macrophages infected by MHV, we showed that ACSL1 constituted the dominant isoform of acyl-CoA synthetase family members. Therefore, Triacsin C was considered as the ACSL1-sepcific inhibitor in our experiments. Two independent compound screening studies showed that Triacsin C can be a candidate for restricting SARS-CoV-2 infection, further validating the involvement of acyl-CoA synthetase family members in coronavirus infection. However, due to the lacking of target specificity, it is challenging for Triacsin C to be applied for the inhibition of ACSL1 *in vivo*. Recently, a compound based on Triacsin C showed highly potent and selective inhibitory effects on ACSL1 (68). This refined compound may be selected as an ideal inhibitor for treatment of coronavirus infection.

Collectively, our study provided the implications for focusing on the correlation between ferroptosis and inflammation in coronavirus infection. Our findings emphasized the importance of acyl-CoA synthetase family members, especially ACSL1 in MHV infection, and showed that ferroptosis inhibition offered benefits for individuals suffering coronavirus infection.

Materials and methods

Cells

RAW 264.7, iBMDM, MEF and 17CL-1 cells were kept in our lab. Mouse alveolar macrophage cell line MH-S cells were from American Type Culture Collection (ATCC). Cells were cultured in Dulbecco's modified eagle medium (DMEM) supplemented with 10% FBS (PAN), 1% glutamine (Gibco), 100 U/ml penicillin and 100 µg/ml streptomycin at 37°C in the incubator ESCO® CCL-170B-8 with the presence of 5% CO_2.

Primary macrophages

For the isolation of mouse primary peritoneal macrophages (PMs), cells were collected from lavage of the peritoneal cavity from mice that were pre-stimulated with thioglycolate (TG) for 3 days. For the isolation of bone marrow derived macrophages (BMDMs), bone marrow was rinsed out of femurs and tibiae of 6-week-old C57BL6/ mice. Cells were cultured with 30 % L929 cell culture supernatant for 3 days. 3 days later, the supernatant was replaced by fresh cell culture medium with 30% L929 cell culture supernatant and maintained for another 3 days. Mature macrophages were harvested by digesting with trypsin-EDTA for 2 minutes and seeded into 24-well plates for further experiments (200 thousand cells per well).

Murine hepatitis virus culture

The murine hepatitis virus A59 strain has been described previously (2). MHV-A59 was propagated in 17CL-1 cells. Briefly, 0.005 multiplicity of infection (MOI) MHV-A59 was added to the supernatant of growing cells. The cell debris and supernatants were collected, resuspended and froze in -80℃ freezer 36 hours later. The supernatant was frozen and thawed for 3 cycles, centrifuged and subpackaged, followed by the assessment of virus titer via plaque assay.

Reagents and drugs

Ferrostatin-1 (HY-100579) and TAK-242 (HY-11109) were from MedChemExpress. Liproxstatin-1 (S81156) was from Yuanye Bio-Tech. Triacsin C (T139793) was from Aladdin. VX-765 (T6090), z-DEVD-FMK (T6005), GSK-872 (T4074), and JSH-23 (T1930) were from Targetmol.

Virus infection in cells

RAW264.7 cells, PMs and BMDMs were infected by MHV-A59 at indicated MOI. 2 hours after infection, the supernatant was removed and cells were covered with culture medium containing compounds at indicated concentration. Infected cells or supernatants were harvested to perform the further experiments.

RNA isolation and RT-qPCR

Total RNA from infected cells was extracted via one-step method using Trizol reagent (Invitrogen) and the cDNA was generated using HiScript II Q RT SuperMix (Vazyme).

Quantitative real-time PCR was carried out using ChamQ Universal SYBR qPCR Master Mix (Vazyme) and specific primers on the 7500 Fast Real-Time PCR Instrument (Applied Biosystems). Data were analyzed using GraphPad Prism Version 8.0 (GraphPad Software) according to the $2^{-\Delta Ct}$ threshold calculation method and means ± SD. The relative RNA expression level was normalized to *Hprt* quantified in parallel amplification reactions. Primer sequences were listed as follows:

m*Hprt*-F: 5'-TCAGTCAACGGGGGACATAAA-3'

m*Hprt*-R: 5'-GGGGCTGTACTGCTTAACCAG-3'

m*Il6*-F: 5'-TCTGCAAGAGACTTCCATCCAGTTGC-3'

m*Il6*-R: 5'-AGCCTCCGACTTGTGAAGTGGT-3'

m*Ifnb1*-F: 5'-TCCGAGCAGAGATCTTCAGGAA-3'

m*Ifnb1*-R: 5'-GCAACCACCACTCATTCTGAG-3'

m*Cxcl10*-F: 5'-CCAAGTGCTGCCGTCATTTTC-3'

m*Cxcl10*-R: 5'-GGCTCGCAGGGATGATTTCAA-3'

m*Acsl1*-F: 5'-TGCCAGAGCTGATTGACATTC-3'

m*Acsl1*-R: 5'-GGCATACCAGAAGGTGGTGAG-3'

MHV-pp-F: 5'-TGCCTGAAACGCATGTTGTG-3'

MHV-pp-R: 5'-CAGACAAACCAGTGTTGGCG-3'

Bulk RNA-seq

Integrity of RNA purified from indicated BMDM or PM samples was assessed using the RNA Nano 6000 Assay Kit of the Agilent Bioanalyzer 2100 system (Agilent Technologies).

All samples showed RNA integrity number > 8. RNA sequencing libraries were generated using NEBNext Ultra Directional RNA Library Prep Kit for Illumina (NEB), and sequenced on an Illumina Novaseq PE150 platform. Sequencing was performed at Genewiz Co. Ltd. The filtered reads were mapped to the mouse genome reference sequence (GRCm38/mm10 Ensembl release 81) using HISAT2. Gene expression was quantified as fragments per kilobase of coding sequence per million reads (FPKM) algorithm. Genes were ranked by log2 of fold change (log2FC) and -log10 of false discovery rate (-log10(FDR)). For the gene ontology analysis, top upregulated genes were uploaded to DAVID Bioinformatics Resources 6.8 to perform Gene Ontology (GO) analysis. Top enriched items ($p < 0.05$) were shown in the figure, as described in the legend of figure 4.

PI staining

Real-time cell membrane permeability assessment was carried out using PI staining. Live cells were covered by cell culture medium with 20 μM PI. Cells were cultured for 15 min followed by washing with PBS for 2 times. Then cells were covered with culture medium and monitored under fluorescence microscope.

Cell imaging

For the imaging under bright field alone, cells were monitored using CytoSMART Lux2 cell imaging system (CytoSMART). Extent of syncytia formation was determined with cell confluence level, which was calculated in CytoSMART website. For the imaging of cells stained with PI, cells were monitored using Olympus IX70 Fluorescence Microscope

(Olympus).

Cytokine measurement and LDH assay

For the detection of cytokine abundance in the cell culture supernatant, supernatants from treated cells were collected to perform ELISA following the manufacturer's instructions. The following ELISA kits was used: mouse IL-6 ELISA kit (Dakewei). LDH was measured via colorimetric NAD linked assay using LDH detection kit (Leagene).

Plaque assay

Virus yield of MHV-A59 in culture supernatants was determined by plaque assay with 17CL-1 cells. Culture supernatant was harvested and diluted to infect confluent 17CL-1 cells cultured in 24-well plates. Viruses were removed 2 hours after infection and cells were washed with pre-warmed PBS followed by culture with DMEM containing 0.5% methylcellulose. After 36 hours of infection, the overlay was removed and cells were fixed with 4% paraformaldehyde for 10 min and stained with 1% crystal violet for 20 min. Plaques were counted, averaged, and multiplied by the dilution factor to determine the viral titer as plaque-forming units per mL (PFU/mL).

Animal model

All mice were bred and maintained in specific pathogen-free (SPF) conditions with approval by the Peking University animal care and use committee. For the infection experiments, 4-week-old C57BL/6 male mice were anesthetized via inhaling isoflurane

and then inoculated intranasally (i.n.) with 10 μL of MHV-A59 virus at 1×10^4 PFU. Mice were intranasally treated daily with Lip-1 or vehicle alone from day 1 to day 10 post infection or mock infection. We monitored the weight of each mouse every day until mice were sacrificed. Mice were sacrificed at day 4 or day 18 post infection or mock infection to evaluate the tissue injury and inflammation caused by MHV-A59 infection.

Histology

Mice were sacrificed at indicated time points after infection. Lungs from each group were fixed with 4% paraformaldehyde, embedded in paraffin and cut into sections of 3.5 μm, and further stained with hematoxylin and eosin (HE). Immune cells infiltration and hemorrhages were determined and evaluated under light microscopy. The images were taken by Leica DM 6B microscope.

Statistical analysis

Results were analyzed by paired or unpaired Student's *t*-test or by two-way ANOVA analysis (for determining the differences in the weight loss curves). GraphPad Prism 8.0 was used for statistical analysis and graphing. Data was shown as mean ± SD unless indicated in the legend. Statistical values can be found in the figure legends. $*p < 0.05$, $**p < 0.01$, $****p < 0.0001$. For experiments *in vivo*, n= number of individual animals.

463 Figure legends

464

465 Figure 1. Ferroptosis inhibitor Fer-1 inhibited MHV-A59 induced syncytia and membrane
466 damage.
467 (A and B) Primary peritoneal macrophages (PMs) were infected with MHV-A59 at 0.05
468 MOI. After 2 hours of infection, cells were treated with Fer-1 (10 μM). After 24 hours of
469 infection, cells were imaged using CytoSMART system (A) and cell confluence was
470 evaluated using the CytoSMART website (B). (C) PMs were infected as described in (A)
471 and were stained with propidium iodide (PI). After staining cells were imaged under
472 fluorescence microscope. (D) PMs were infected as described in (A), followed by the
473 treatment with Fer-1 (10 μM), z-DEVD-FMK (25 μM), VX-765 (30 μM) or GSK-872 (10 μM).
474 Cells were stained with PI and imaged under fluorescence microscope. (E) Scale bars:
475 For (A) and (C), 200 μm. For (D), 100 μm. Data from two independent experiments was
476 shown. *, $p < 0.05$; Student's *t*-test. See also Video S1.

477

478 Figure 2. Fer-1 inhibited MHV-A59 propagation and infection induced inflammatory
479 cytokine and LDH release.
480 (A) PMs or BMDMs were infected with MHV-A59 at 0.05 MOI for 24 hours. Fer-1 was
481 added after 2 hours of infection. MHV abundance was evaluated by the expression of
482 MHV polyprotein (MHV-pp). MHV-pp expression was tested by qRT-PCR. (B) Viral load of
483 MHV-A59 from supernatants of PMs from (A) was evaluated with plaque assay. (C and D)
484 Expression of *Il6*, *Cxcl10* and *Ifnb1* after MHV infection in PMs (C) or BMDMs (D) with or

485 without Fer-1 treatment was tested by qRT-PCR. (E) IL-6 abundance from supernatants of
486 PMs from (C) was tested with ELISA. (F) Percentage of LDH release of PMs from (C) was
487 tested by LDH detection kit. Data from two independent experiments was shown. **, $p <$
488 0.01; ****, $p < 0.0001$; Student's t-test. NS, not significant. See also Figure S1.
489
490 Figure 3. Lip-1 alleviated MHV induced lung tissue injury.
491 (A) Diagram of MHV-A59 infection model. 4-week-old male C57BL/6 mice were infected
492 intranasally (i.n.) with 1 x 10^5 PFU MHV-A59 in 10 μL DMEM. Lip-1 (10 mg/kg) was
493 inhaled daily from day 1 to day 10 post infection. Mice were sacrificed at day 4 post
494 infection and lung tissues were collected and processed to perform HE staining.
495 Remained mice were sacrificed at day 18 post infection, which was the end point of the
496 infection model. Lung tissues were collected, photographed and processed to perform HE
497 staining. Body weight changes of mice was monitored through the entire infection period.
498 (B) Photograph of lung tissues collected at day 18 post infection. Black arrows indicated
499 obvious hemorrhagic alterations. (C) HE staining of lung tissues collected at day 4 post
500 infection. Black arrows indicated obvious hemorrhagic alterations. Black asterisks
501 indicated immune cells infiltration. (D) HE staining of lung tissues collected at day 18 post
502 infection. See also in Figure S2.
503
504 Figure 4. MHV-A59 infection upregulated NF-κB dependent *Acsl1* expression.
505 (A and B) BMDMs were infected by MHV-A59 at 0.1 MOI for 12 hours and RNA was
506 isolated to perform bulk RNA-seq. Top upregulated genes were uploaded to DAVID

Bioinformatics Resources 6.8 to perform Gene Ontology analysis. Top enriched items (p < 0.05) were shown in (A). Expression changes of all genes (MHV infected versus control cells) was shown in (B), ranked by log2 fold change (log2FC) and –log10(false discovery rate) (-log10(FDR)). Dot of *Acsl1* was marked with red. (C) Expression of acyl-CoA synthetase long-chain family members from (A) was compared via qRT-PCR. (D) Expression changes of all genes from BMDMs after MHV infection was shown. Dot of *Acsl1* was marked with red. (E) Expression of *Ptgs2* in (D) was shown. (F) Expression of *Acsl1* after MHV-A59 infection in various cell lines was tested. (G and H) Impacts of TAK-242 (1 μM) (G) or JSH-23 (20 μM) (H) on the expression of *Acsl1* after MHV-A59 infection in PMs. Data from two independent experiments was shown. *, p < 0.05; **, p < 0.01; Student's *t*-test.

Figure 5. Triacsin C inhibited MHV propagation and infection induced syncytia formation. (A and B) Viral load of MHV-A59 from supernatants of PMs (A) or BMDMs (B) after Lip-1 (10 μM) or Triacsin C (2 μM) treatment. (C and D) Expression of *Il6*, *Cxcl10* and *Ifnb1* after MHV infection in PMs (C) or BMDMs (D) after Fer-1 (10 μM) or Triacsin C (2 μM) treatment was tested by qRT-PCR. (E and F) PMs were infected by MHV-A59 followed by treatment with Fer-1 (10 μM) or Triacsin C (2 μM). After 24 hours of infection, PMs were imaged using CytoSMART system (E) and cell confluence was evaluated using the CytoSMART website (F). Scale bars: 200 μm. Data from two independent experiments was shown. *, p < 0.05; **, p < 0.01; Student's *t*-test. See also Figure S3.

Figure S1. Fer-1 does not inhibit viral entry of MHV-A59.

Referring to Figure 2. PMs were pre-treated with Fer-1 (10 μM) for 2 hours and infected with MHV-A59 at 1 MOI for 2 hours. Expression of MHV-pp was tested by qRT-PCR. NS, not significant.

Figure S2. Lip-1 was not able to reverse reduced gain of body weights in low-dose MHV-A59 infection model.

Referring to Figure 3. Body weight changes were monitored daily. Apparent restriction of gain of body weight compared with non-infected group was observed after MHV-A59 infection. Data was shown as means ± SEM. **, $p < 0.01$; Student's *t*-test. NS, not significant.

Figure S3. RAW 264.7 cells were not protected from ferroptosis inhibition after MHV-A59 infection.

(A) RAW 264.7 cells were infected with MHV-A59 at 0.05 MOI for 24 hours, stained with PI and imaged under fluorescence microscope. RAW 264.7 cells showed no obvious membrane permeability alterations after MHV-A59 infection.

(B and C) RAW 264.7 cells were infected with MHV-A59 at 0.05 MOI for 24 hours. Expression of *Ifnb1* (B) and MHV-pp (C) was tested by qRT-PCR.

(D) Viral load of MHV-A59 from supernatants of RAW 264.7 cells with or without Fer-1 (10 μM) treatment. NS, not significant.

Figure S4. Triacsin C inhibited MHV induced syncytia formation in BMDM.

Referring to Figure 5. Impacts of Fer-1 (10 μM) or Triacsin C (2 μM) on syncytia formation of BMDMs after MHV-A59 infection. Black arrows indicated cell syncytia.

Video S1. MHV-A59 infection induced ferroptosis-like morphological changes of murine peritoneal macrophages

Referring to Figure 1. PMs were infected with MHV-A59 at 0.1 MOI. Cell morphology was monitored under CytoSMART Live Cell Imaging System for 24 hours.

Acknowledgments

We thank Dr. Zhao Yingchi for help refining the viral propagation experiments. This work was supported by the National Key Research and Development Program of China (2016YFA0500300; 2020YFA0707800), the National Natural Science Foundation of China (31570891; 31872736; 32022028; 81991505), Peking University Clinical+X (PKU2020LCXQ009), the Peking University Medicine Fund (PKU2020LCXQ009.

Author contributions

F.Y. and Z.Z. designed the research; X.H. and Z.Z. performed the experiments and analyzed data; F.Y. supervised the study; Z.Z., X.H. and F.Y. interpreted data and wrote the manuscript. All authors commented on the manuscript.

573

574 Competing interests

575 The authors declare that they have no competing interests.

576

577 Data and materials availability

578 The raw data of RNA sequencing in this publication has been deposited in NCBI's Gene
579 Expression Omnibus and are accessible through GEO Series accession numbers
580 GSE185800.

581

582 Abbreviations

583 Murine hepatitis virus strain A59, MHV-A59; damage-associated molecular pattern
584 molecule, DAMP; coronavirus disease 2019, COVID-19; reactive oxygen species, ROS;
585 new castle virus, NDV; bone marrow derived macrophage, BMDM; peritoneal
586 macrophages, PMs; ferrostatin-1, Fer-1; liproxstatin-1, Lip-1.

587

588

589

590 References

591 [1] Lavi E, Gilden DH, Wroblewska Z, Rorke LB and Weiss SR. Experimental
592 demyelination produced by the A59 strain of mouse hepatitis virus. Neurology. 1984,
593 34(5): 597-603

594 [2] Yang Z, Du J, Chen G, Zhao J, Yang X, Su L, Cheng G and Tang H. Coronavirus

595 MHV-A59 infects the lung and causes severe pneumonia in C57BL/6 mice. Virol Sin. 2014,
596 29(6): 393-402
597 [3] Ryu S, Shchukina I, Youm YH, Qing H, Hilliard B, Dlugos T, Zhang X, Yasumoto Y,
598 Booth CJ, Fernández-Hernando C, Suárez Y, Khanna K, Horvath TL, Dietrich MO,
599 Artyomov M, Wang A and Dixit VD. Ketogenic diet restrains aging-induced exacerbation
600 of coronavirus infection in mice. Elife. 2021, 10:
601 [4] Guo Q, Zhao Y, Li J, Liu J, Yang X, Guo X, Kuang M, Xia H, Zhang Z, Cao L, Luo Y,
602 Bao L, Wang X, Wei X, Deng W, Wang N, Chen L, Chen J, Zhu H, Gao R, Qin C, Wang X
603 and You F. Induction of alarmin S100A8/A9 mediates activation of aberrant neutrophils in
604 the pathogenesis of COVID-19. Cell Host Microbe. 2021, 29(2): 222-235.e224
605 [5] Dixon SJ, Lemberg KM, Lamprecht MR, Skouta R, Zaitsev EM, Gleason CE, Patel DN,
606 Bauer AJ, Cantley AM, Yang WS, Morrison B, 3rd and Stockwell BR. Ferroptosis: an
607 iron-dependent form of nonapoptotic cell death. Cell. 2012, 149(5): 1060-1072
608 [6] Yang WS, Kim KJ, Gaschler MM, Patel M, Shchepinov MS and Stockwell BR.
609 Peroxidation of polyunsaturated fatty acids by lipoxygenases drives ferroptosis. Proc Natl
610 Acad Sci U S A. 2016, 113(34): E4966-4975
611 [7] Wenzel SE, Tyurina YY, Zhao J, St Croix CM, Dar HH, Mao G, Tyurin VA,
612 Anthonymuthu TS, Kapralov AA, Amoscato AA, Mikulska-Ruminska K, Shrivastava IH,
613 Kenny EM, Yang Q, Rosenbaum JC, Sparvero LJ, Emlet DR, Wen X, Minami Y, Qu F,
614 Watkins SC, Holman TR, VanDemark AP, Kellum JA, Bahar I, Bayır H and Kagan VE.
615 PEBP1 Wardens Ferroptosis by Enabling Lipoxygenase Generation of Lipid Death
616 Signals. Cell. 2017, 171(3): 628-641.e626

617 [8] Friedmann Angeli JP, Schneider M, Proneth B, Tyurina YY, Tyurin VA, Hammond VJ,
618 Herbach N, Aichler M, Walch A, Eggenhofer E, Basavarajappa D, Rådmark O, Kobayashi
619 S, Seibt T, Beck H, Neff F, Esposito I, Wanke R, Förster H, Yefremova O, Heinrichmeyer
620 M, Bornkamm GW, Geissler EK, Thomas SB, Stockwell BR, O'Donnell VB, Kagan VE,
621 Schick JA and Conrad M. Inactivation of the ferroptosis regulator Gpx4 triggers acute
622 renal failure in mice. Nat Cell Biol. 2014, 16(12): 1180-1191
623 [9] Bersuker K, Hendricks JM, Li Z, Magtanong L, Ford B, Tang PH, Roberts MA, Tong B,
624 Maimone TJ, Zoncu R, Bassik MC, Nomura DK, Dixon SJ and Olzmann JA. The CoQ
625 oxidoreductase FSP1 acts parallel to GPX4 to inhibit ferroptosis. Nature. 2019, 575(7784):
626 688-692
627 [10] Doll S, Freitas FP, Shah R, Aldrovandi M, da Silva MC, Ingold I, Goya Grocin A,
628 Xavier da Silva TN, Panzilius E, Scheel CH, Mourão A, Buday K, Sato M, Wanninger J,
629 Vignane T, Mohana V, Rehberg M, Flatley A, Schepers A, Kurz A, White D, Sauer M,
630 Sattler M, Tate EW, Schmitz W, Schulze A, O'Donnell V, Proneth B, Popowicz GM, Pratt
631 DA, Angeli JPF and Conrad M. FSP1 is a glutathione-independent ferroptosis suppressor.
632 Nature. 2019, 575(7784): 693-698
633 [11] Dixon SJ, Patel DN, Welsch M, Skouta R, Lee ED, Hayano M, Thomas AG, Gleason
634 CE, Tatonetti NP, Slusher BS and Stockwell BR. Pharmacological inhibition of
635 cystine-glutamate exchange induces endoplasmic reticulum stress and ferroptosis. Elife.
636 2014, 3: e02523
637 [12] Doll S, Proneth B, Tyurina YY, Panzilius E, Kobayashi S, Ingold I, Irmler M, Beckers J,
638 Aichler M, Walch A, Prokisch H, Trümbach D, Mao G, Qu F, Bayir H, Füllekrug J, Scheel

639 CH, Wurst W, Schick JA, Kagan VE, Angeli JP and Conrad M. ACSL4 dictates ferroptosis
640 sensitivity by shaping cellular lipid composition. Nat Chem Biol. 2017, 13(1): 91-98
641 [13] Kagan VE, Mao G, Qu F, Angeli JP, Doll S, Croix CS, Dar HH, Liu B, Tyurin VA, Ritov
642 VB, Kapralov AA, Amoscato AA, Jiang J, Anthonymuthu T, Mohammadyani D, Yang Q,
643 Proneth B, Klein-Seetharaman J, Watkins S, Bahar I, Greenberger J, Mallampalli RK,
644 Stockwell BR, Tyurina YY, Conrad M and Bayır H. Oxidized arachidonic and adrenic PEs
645 navigate cells to ferroptosis. Nat Chem Biol. 2017, 13(1): 81-90
646 [14] Yuan H, Li X, Zhang X, Kang R and Tang D. Identification of ACSL4 as a biomarker
647 and contributor of ferroptosis. Biochem Biophys Res Commun. 2016, 478(3): 1338-1343
648 [15] Beatty A, Singh T, Tyurina YY, Tyurin VA, Samovich S, Nicolas E, Maslar K, Zhou Y,
649 Cai KQ, Tan Y, Doll S, Conrad M, Subramanian A, Bayır H, Kagan VE, Rennefahrt U and
650 Peterson JR. Ferroptotic cell death triggered by conjugated linolenic acids is mediated by
651 ACSL1. Nat Commun. 2021, 12(1): 2244
652 [16] Al-Rashed F, Thomas R, Al-Roub A, Al-Mulla F and Ahmad R. LPS Induces GM-CSF
653 Production by Breast Cancer MDA-MB-231 Cells via Long-Chain Acyl-CoA Synthetase 1.
654 Molecules. 2020, 25(20):
655 [17] Jorgensen I, Rayamajhi M and Miao EA. Programmed cell death as a defence against
656 infection. Nat Rev Immunol. 2017, 17(3): 151-164
657 [18] Karki R, Sharma BR, Tuladhar S, Williams EP, Zalduondo L, Samir P, Zheng M,
658 Sundaram B, Banoth B, Malireddi RKS, Schreiner P, Neale G, Vogel P, Webby R,
659 Jonsson CB and Kanneganti TD. Synergism of TNF-α and IFN-γ Triggers Inflammatory
660 Cell Death, Tissue Damage, and Mortality in SARS-CoV-2 Infection and Cytokine Shock

661 Syndromes. Cell. 2021, 184(1): 149-168.e117

662 [19] Zheng M, Williams EP, Malireddi RKS, Karki R, Banoth B, Burton A, Webby R,

663 Channappanavar R, Jonsson CB and Kanneganti TD. Impaired NLRP3 inflammasome

664 activation/pyroptosis leads to robust inflammatory cell death via caspase-8/RIPK3 during

665 coronavirus infection. J Biol Chem. 2020, 295(41): 14040-14052

666 [20] Li S, Zhang Y, Guan Z, Li H, Ye M, Chen X, Shen J, Zhou Y, Shi ZL, Zhou P and

667 Peng K. SARS-CoV-2 triggers inflammatory responses and cell death through caspase-8

668 activation. Signal Transduct Target Ther. 2020, 5(1): 235

669 [21] Ferreira AC, Soares VC, de Azevedo-Quintanilha IG, Dias S, Fintelman-Rodrigues N,

670 Sacramento CQ, Mattos M, de Freitas CS, Temerozo JR, Teixeira L, Damaceno Hottz E,

671 Barreto EA, Pão CRR, Palhinha L, Miranda M, Bou-Habib DC, Bozza FA, Bozza PT and

672 Souza TML. SARS-CoV-2 engages inflammasome and pyroptosis in human primary

673 monocytes. Cell Death Discov. 2021, 7(1): 43

674 [22] Ma H, Zhu Z, Lin H, Wang S, Zhang P, Li Y, Li L, Wang J, Zhao Y and Han J.

675 Pyroptosis of syncytia formed by fusion of SARS-CoV-2 spike and ACE2-expressing cells.

676 Cell Discov. 2021, 7(1): 73

677 [23] Kan X, Yin Y, Song C, Tan L, Qiu X, Liao Y, Liu W, Meng S, Sun Y and Ding C.

678 Newcastle-disease-virus-induced ferroptosis through nutrient deprivation and

679 ferritinophagy in tumor cells. iScience. 2021, 24(8): 102837

680 [24] Armitage AE, Stacey AR, Giannoulatou E, Marshall E, Sturges P, Chatha K, Smith

681 NM, Huang X, Xu X, Pasricha SR, Li N, Wu H, Webster C, Prentice AM, Pellegrino P,

682 Williams I, Norris PJ, Drakesmith H and Borrow P. Distinct patterns of hepcidin and iron

683 regulation during HIV-1, HBV, and HCV infections. Proc Natl Acad Sci U S A. 2014,
684 111(33): 12187-12192
685 [25] Chow JK, Werner BG, Ruthazer R and Snydman DR. Increased serum iron levels
686 and infectious complications after liver transplantation. Clin Infect Dis. 2010, 51(3): e16-23
687 [26] Jia M, Qin D, Zhao C, Chai L, Yu Z, Wang W, Tong L, Lv L, Wang Y, Rehwinkel J, Yu
688 J and Zhao W. Redox homeostasis maintained by GPX4 facilitates STING activation. Nat
689 Immunol. 2020, 21(7): 727-735
690 [27] Li P, Jiang M, Li K, Li H, Zhou Y, Xiao X, Xu Y, Krishfield S, Lipsky PE, Tsokos GC
691 and Zhang X. Glutathione peroxidase 4-regulated neutrophil ferroptosis induces systemic
692 autoimmunity. Nat Immunol. 2021, 22(9): 1107-1117
693 [28] Yao Y, Chen Z, Zhang H, Chen C, Zeng M, Yunis J, Wei Y, Wan Y, Wang N, Zhou M,
694 Qiu C, Zeng Q, Ong HS, Wang H, Makota FV, Yang Y, Yang Z, Wang N, Deng J, Shen C,
695 Xia Y, Yuan L, Lian Z, Deng Y, Guo C, Huang A, Zhou P, Shi H, Zhang W, Yi H, Li D, Xia
696 M, Fu J, Wu N, de Haan JB, Shen N, Zhang W, Liu Z and Yu D. Selenium-GPX4 axis
697 protects follicular helper T cells from ferroptosis. Nat Immunol. 2021, 22(9): 1127-1139
698 [29] Wen Q, Liu J, Kang R, Zhou B and Tang D. The release and activity of HMGB1 in
699 ferroptosis. Biochem Biophys Res Commun. 2019, 510(2): 278-283
700 [30] Liu Y, Wang Y, Liu J, Kang R and Tang D. The circadian clock protects against
701 ferroptosis-induced sterile inflammation. Biochem Biophys Res Commun. 2020, 525(3):
702 620-625
703 [31] Huang L, Shi Y, Gong B, Jiang L, Zhang Z, Liu X, Yang J, He Y, Jiang Z, Zhong L,
704 Tang J, You C, Jiang Q, Long B, Zeng T, Luo M, Zeng F, Zeng F, Wang S, Yang X and

705 Yang Z. Dynamic blood single-cell immune responses in patients with COVID-19. Signal
706 Transduct Target Ther. 2021, 6(1): 110
707 [32] Girelli D, Marchi G, Busti F and Vianello A. Iron metabolism in infections: Focus on
708 COVID-19. Semin Hematol. 2021, 58(3): 182-187
709 [33] Yang M and Lai CL. SARS-CoV-2 infection: can ferroptosis be a potential treatment
710 target for multiple organ involvement? Cell Death Discov. 2020, 6: 130
711 [34] Zhao K, Huang J, Dai D, Feng Y, Liu L and Nie S. Serum Iron Level as a Potential
712 Predictor of Coronavirus Disease 2019 Severity and Mortality: A Retrospective Study.
713 Open Forum Infect Dis. 2020, 7(7): ofaa250
714 [35] Chakurkar V, Rajapurkar M, Lele S, Mukhopadhyay B, Lobo V, Injarapu R, Sheikh M,
715 Dholu B, Ghosh A and Jha V. Increased serum catalytic iron may mediate tissue injury
716 and death in patients with COVID-19. Sci Rep. 2021, 11(1): 19618
717 [36] Wang Y, Huang J, Sun Y, Stubbs D, He J, Li W, Wang F, Liu Z, Ruzicka JA, Taylor
718 EW, Rayman MP, Wan X and Zhang J. SARS-CoV-2 suppresses mRNA expression of
719 selenoproteins associated with ferroptosis, endoplasmic reticulum stress and DNA
720 synthesis. Food Chem Toxicol. 2021, 153: 112286
721 [37] Buchrieser J, Dufloo J, Hubert M, Monel B, Planas D, Rajah MM, Planchais C, Porrot
722 F, Guivel-Benhassine F, Van der Werf S, Casartelli N, Mouquet H, Bruel T and Schwartz
723 O. Syncytia formation by SARS-CoV-2-infected cells. Embo j. 2020, 39(23): e106267
724 [38] Sanders DW, Jumper CC, Ackerman PJ, Bracha D, Donlic A, Kim H, Kenney D,
725 Castello-Serrano I, Suzuki S, Tamura T, Tavares AH, Saeed M, Holehouse AS, Ploss A,
726 Levental I, Douam F, Padera RF, Levy BD and Brangwynne CP. SARS-CoV-2 requires

727 cholesterol for viral entry and pathological syncytia formation. Elife. 2021, 10:

728 [39] Daniloski Z, Jordan TX, Wessels HH, Hoagland DA, Kasela S, Legut M, Maniatis S,

729 Mimitou EP, Lu L, Geller E, Danziger O, Rosenberg BR, Phatnani H, Smibert P,

730 Lappalainen T, tenOever BR and Sanjana NE. Identification of Required Host Factors for

731 SARS-CoV-2 Infection in Human Cells. Cell. 2021, 184(1): 92-105.e116

732 [40] Lamers MM, Beumer J, van der Vaart J, Knoops K, Puschhof J, Breugem TI, Ravelli

733 RBG, Paul van Schayck J, Mykytyn AZ, Duimel HQ, van Donselaar E, Riesebosch S,

734 Kuijpers HJH, Schipper D, van de Wetering WJ, de Graaf M, Koopmans M, Cuppen E,

735 Peters PJ, Haagmans BL and Clevers H. SARS-CoV-2 productively infects human gut

736 enterocytes. Science. 2020, 369(6499): 50-54

737 [41] Grant RA, Morales-Nebreda L, Markov NS, Swaminathan S, Querrey M, Guzman ER,

738 Abbott DA, Donnelly HK, Donayre A, Goldberg IA, Klug ZM, Borkowski N, Lu Z, Kihshen H,

739 Politanska Y, Sichizya L, Kang M, Shilatifard A, Qi C, Lomasney JW, Argento AC, Kruser

740 JM, Malsin ES, Pickens CO, Smith SB, Walter JM, Pawlowski AE, Schneider D,

741 Nannapaneni P, Abdala-Valencia H, Bharat A, Gottardi CJ, Budinger GRS, Misharin AV,

742 Singer BD and Wunderink RG. Circuits between infected macrophages and T cells in

743 SARS-CoV-2 pneumonia. Nature. 2021, 590(7847): 635-641

744 [42] Williams RK, Jiang GS and Holmes KV. Receptor for mouse hepatitis virus is a

745 member of the carcinoembryonic antigen family of glycoproteins. Proc Natl Acad Sci U S

746 A. 1991, 88(13): 5533-5536

747 [43] Cantuti-Castelvetri L, Ojha R, Pedro LD, Djannatian M, Franz J, Kuivanen S, van der

748 Meer F, Kallio K, Kaya T, Anastasina M, Smura T, Levanov L, Szirovicza L, Tobi A,

749 Kallio-Kokko H, Österlund P, Joensuu M, Meunier FA, Butcher SJ, Winkler MS,
750 Mollenhauer B, Helenius A, Gokce O, Teesalu T, Hepojoki J, Vapalahti O, Stadelmann C,
751 Balistreri G and Simons M. Neuropilin-1 facilitates SARS-CoV-2 cell entry and infectivity.
752 Science. 2020, 370(6518): 856-860
753 [44] Daly JL, Simonetti B, Klein K, Chen KE, Williamson MK, Antón-Plágaro C, Shoemark
754 DK, Simón-Gracia L, Bauer M, Hollandi R, Greber UF, Horvath P, Sessions RB, Helenius
755 A, Hiscox JA, Teesalu T, Matthews DA, Davidson AD, Collins BM, Cullen PJ and
756 Yamauchi Y. Neuropilin-1 is a host factor for SARS-CoV-2 infection. Science. 2020,
757 370(6518): 861-865
758 [45] Gao J, Mei H, Sun J, Li H, Huang Y, Tang Y, Duan L, Liu D, Wang Q, Gao Y, Song K,
759 Zhao J, Zhang C and Liu J. Neuropilin-1 Mediates SARS-CoV-2 Infection in Bone
760 Marrow-derived Macrophages. bioRxiv. 2021: 2021.2004.2014.439793
761 [46] Zilka O, Shah R, Li B, Friedmann Angeli JP, Griesser M, Conrad M and Pratt DA. On
762 the Mechanism of Cytoprotection by Ferrostatin-1 and Liproxstatin-1 and the Role of Lipid
763 Peroxidation in Ferroptotic Cell Death. ACS Cent Sci. 2017, 3(3): 232-243
764 [47] Miotto G, Rossetto M, Di Paolo ML, Orian L, Venerando R, Roveri A, Vučković AM,
765 Bosello Travain V, Zaccarin M, Zennaro L, Maiorino M, Toppo S, Ursini F and Cozza G.
766 Insight into the mechanism of ferroptosis inhibition by ferrostatin-1. Redox Biol. 2020, 28:
767 101328
768 [48] Chen X, Kang R, Kroemer G and Tang D. Ferroptosis in infection, inflammation, and
769 immunity. Journal of Experimental Medicine. 2021, 218(6):
770 [49] Li Q, Han X, Lan X, Gao Y, Wan J, Durham F, Cheng T, Yang J, Wang Z, Jiang C,

771 Ying M, Koehler RC, Stockwell BR and Wang J. Inhibition of neuronal ferroptosis protects
772 hemorrhagic brain. JCI Insight. 2017, 2(7): e90777
773 [50] Roelands J, Garand M, Hinchcliff E, Ma Y, Shah P, Toufiq M, Alfaki M, Hendrickx W,
774 Boughorbel S, Rinchai D, Jazaeri A, Bedognetti D and Chaussabel D. Long-Chain
775 Acyl-CoA Synthetase 1 Role in Sepsis and Immunity: Perspectives From a Parallel
776 Review of Public Transcriptome Datasets and of the Literature. Front Immunol. 2019, 10:
777 2410
778 [51] Rubinow KB, Wall VZ, Nelson J, Mar D, Bomsztyk K, Askari B, Lai MA, Smith KD,
779 Han MS, Vivekanandan-Giri A, Pennathur S, Albert CJ, Ford DA, Davis RJ and Bornfeldt
780 KE. Acyl-CoA synthetase 1 is induced by Gram-negative bacteria and lipopolysaccharide
781 and is required for phospholipid turnover in stimulated macrophages. J Biol Chem. 2013,
782 288(14): 9957-9970
783 [52] Huang YL, Morales-Rosado J, Ray J, Myers TG, Kho T, Lu M and Munford RS.
784 Toll-like receptor agonists promote prolonged triglyceride storage in macrophages. J Biol
785 Chem. 2014, 289(5): 3001-3012
786 [53] Yang G, Wang Y, Feng J, Liu Y, Wang T, Zhao M, Ye L and Zhang X. Aspirin
787 suppresses the abnormal lipid metabolism in liver cancer cells via disrupting an
788 NFκB-ACSL1 signaling. Biochem Biophys Res Commun. 2017, 486(3): 827-832
789 [54] Santos-Beneit F, Raškevičius V, Skeberdis VA and Bordel S. A metabolic modeling
790 approach reveals promising therapeutic targets and antiviral drugs to combat COVID-19.
791 Sci Rep. 2021, 11(1): 11982
792 [55] Williams CG, Jureka AS, Silvas JA, Nicolini AM, Chvatal SA, Carlson-Stevermer J,

793 Oki J, Holden K and Basler CF. Inhibitors of VPS34 and fatty-acid metabolism suppress
794 SARS-CoV-2 replication. Cell Rep. 2021, 36(5): 109479
795 [56] Ren G, Bhatnagar S, Hahn DJ and Kim JA. Long-chain acyl-CoA synthetase-1
796 mediates the palmitic acid-induced inflammatory response in human aortic endothelial
797 cells. Am J Physiol Endocrinol Metab. 2020, 319(5): E893-e903
798 [57] Li X, Wang TX, Huang X, Li Y, Sun T, Zang S, Guan KL, Xiong Y, Liu J and Yuan HX.
799 Targeting ferroptosis alleviates methionine-choline deficient (MCD)-diet induced NASH by
800 suppressing liver lipotoxicity. Liver Int. 2020, 40(6): 1378-1394
801 [58] Li N, Wang W, Zhou H, Wu Q, Duan M, Liu C, Wu H, Deng W, Shen D and Tang Q.
802 Ferritinophagy-mediated ferroptosis is involved in sepsis-induced cardiac injury. Free
803 Radic Biol Med. 2020, 160: 303-318
804 [59] Matsushita M, Freigang S, Schneider C, Conrad M, Bornkamm GW and Kopf M. T
805 cell lipid peroxidation induces ferroptosis and prevents immunity to infection. J Exp Med.
806 2015, 212(4): 555-568
807 [60] Amaral EP, Costa DL, Namasivayam S, Riteau N, Kamenyeva O, Mittereder L,
808 Mayer-Barber KD, Andrade BB and Sher A. A major role for ferroptosis in Mycobacterium
809 tuberculosis-induced cell death and tissue necrosis. J Exp Med. 2019, 216(3): 556-570
810 [61] Bartolini D, Stabile AM, Bastianelli S, Giustarini D, Pierucci S, Busti C, Vacca C,
811 Gidari A, Francisci D, Castronari R, Mencacci A, Di Cristina M, Focaia R, Sabbatini S,
812 Rende M, Gioiello A, Cruciani G, Rossi R and Galli F. SARS-CoV2 infection impairs the
813 metabolism and redox function of cellular glutathione. Redox Biol. 2021, 45: 102041
814 [62] Ibrahim H, Perl A, Smith D, Lewis T, Kon Z, Goldenberg R, Yarta K, Staniloae C and

815 Williams M. Therapeutic blockade of inflammation in severe COVID-19 infection with
816 intravenous N-acetylcysteine. Clin Immunol. 2020, 219: 108544
817 [63] de Alencar JCG, Moreira CL, Müller AD, Chaves CE, Fukuhara MA, da Silva EA,
818 Miyamoto MFS, Pinto VB, Bueno CG, Lazar Neto F, Gomez Gomez LM, Menezes MCS,
819 Marchini JFM, Marino LO, Brandão Neto RA and Souza HP. Double-blind, Randomized,
820 Placebo-controlled Trial With N-acetylcysteine for Treatment of Severe Acute Respiratory
821 Syndrome Caused by Coronavirus Disease 2019 (COVID-19). Clin Infect Dis. 2021,
822 72(11): e736-e741
823 [64] Kanter JE and Bornfeldt KE. Inflammation and diabetes-accelerated atherosclerosis:
824 myeloid cell mediators. Trends Endocrinol Metab. 2013, 24(3): 137-144
825 [65] Chu J, Xing C, Du Y, Duan T, Liu S, Zhang P, Cheng C, Henley J, Liu X, Qian C, Yin
826 B, Wang HY and Wang RF. Pharmacological inhibition of fatty acid synthesis blocks
827 SARS-CoV-2 replication. Nat Metab. 2021: 1-10
828 [66] Bleau C, Burnette M, Filliol A, Piquet-Pellorce C, Samson M and Lamontagne L.
829 Toll-like receptor-2 exacerbates murine acute viral hepatitis. Immunology. 2016, 149(2):
830 204-224
831 [67] Hayashi K, Kondo N, Omori N, Yoshimoto R, Hato M, Shigaki S, Nagasawa A, Ito M
832 and Okuno T. Discovery of a benzimidazole series as the first highly potent and selective
833 ACSL1 inhibitors. Bioorg Med Chem Lett. 2021, 33: 127722

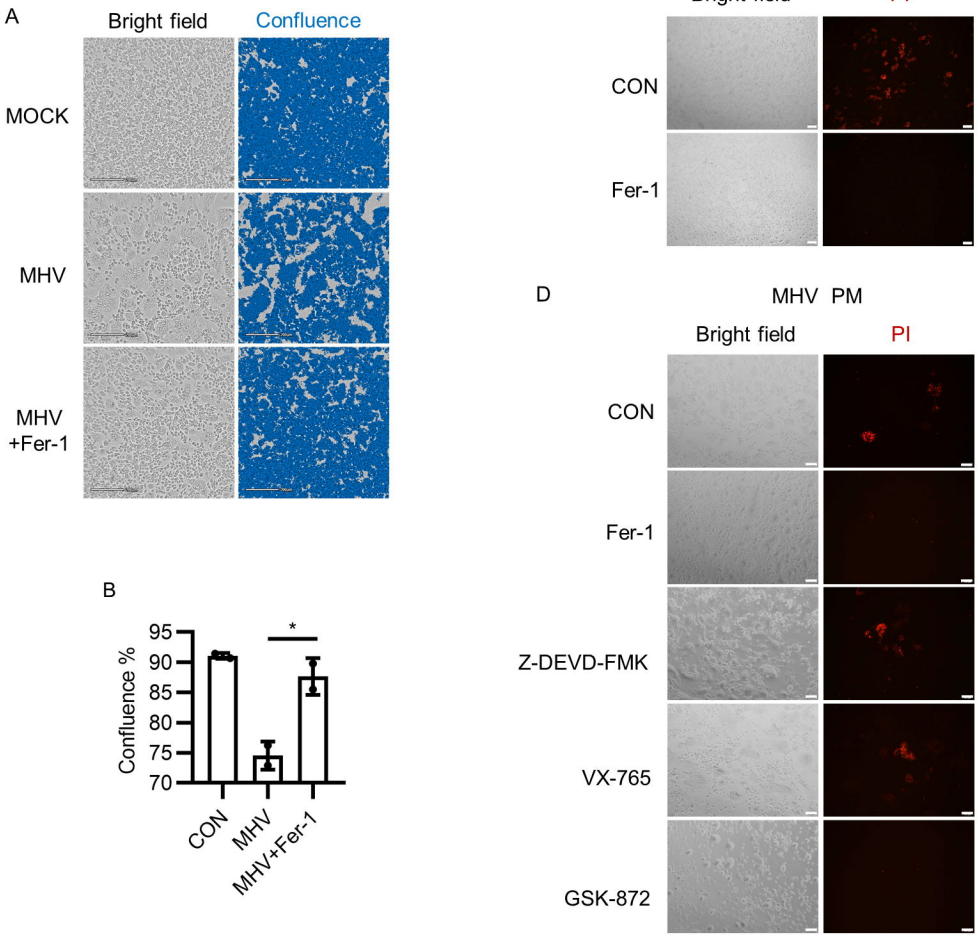
A
Bright field
Confluence
MOCK
MHV
MHV
+Fer-1
B
Confluence %
95
90
85
80
75
70
*
CON
MHV
MHV+Fer-1
C
MHV PM
Bright field
PI
CON
Fer-1
D
MHV PM
Bright field
PI
CON
Fer-1
Z-DEVD-FMK
VX-765
GSK-872

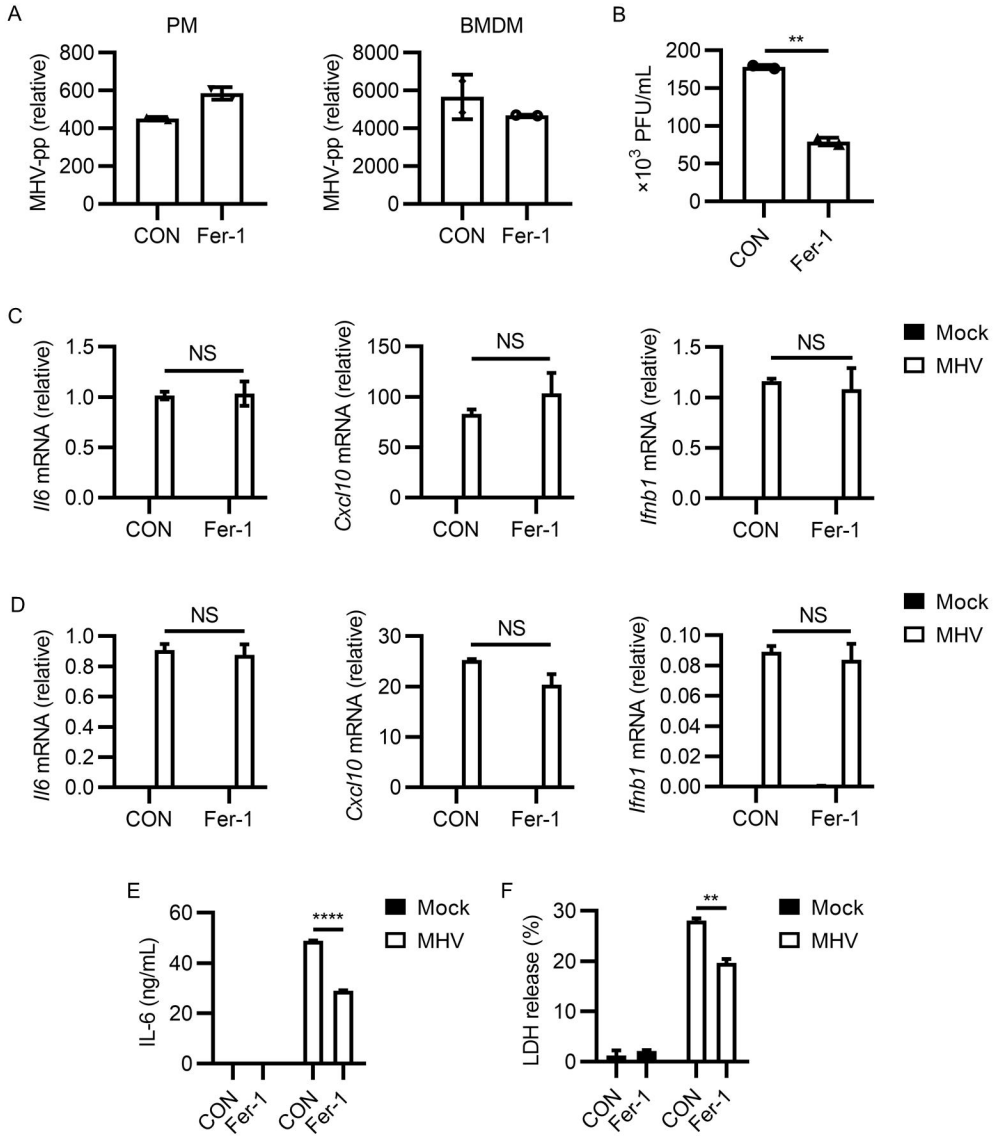
A
PM
BMDM
MHV-pp (relative)
800
600
400
200
0
8000
6000
4000
2000
CON
Fer-1
B
**
×10³ PFU/mL
200
150
100
50
C
NS
Il6 mRNA (relative)
1.5
1.0
0.5
0.0
Cxcl10 mRNA (relative)
150
100
50
Ifnb1 mRNA (relative)
Mock
MHV
D
0.10
0.08
0.06
0.04
0.02
0.00
30
20
10
E
****
IL-6 (ng/mL)
60
40
F
LDH release (%)

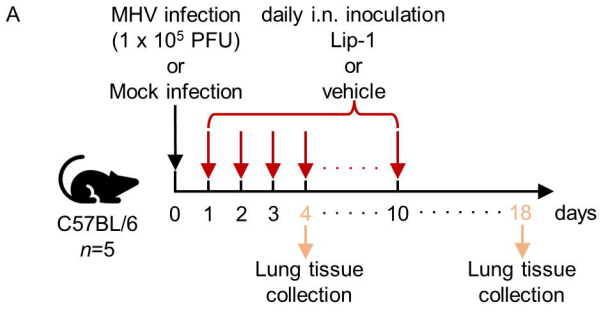
A
MHV infection
(1 x 10^5 PFU)
or
Mock infection
daily i.n. inoculation
Lip-1
or
vehicle
C57BL/6
n=5
0 1 2 3 4 ····· 10 ····· 18 days
Lung tissue collection
Lung tissue collection

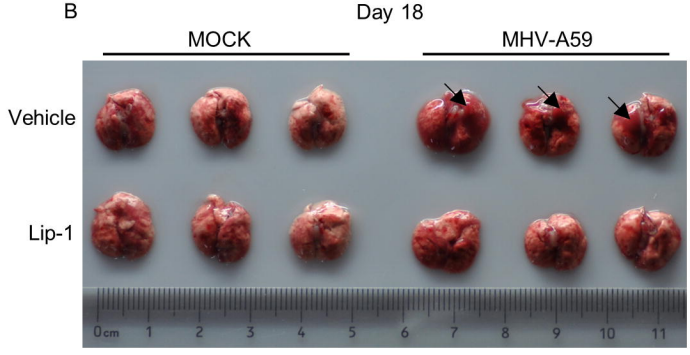
B
Day 18
MOCK
MHV-A59
Vehicle
Lip-1

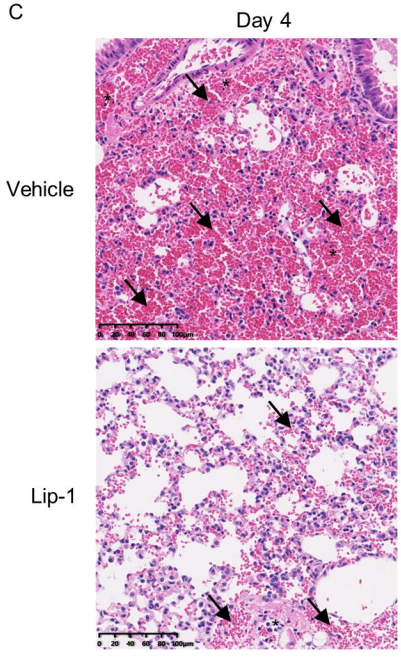
C
Day 4
Vehicle
Lip-1

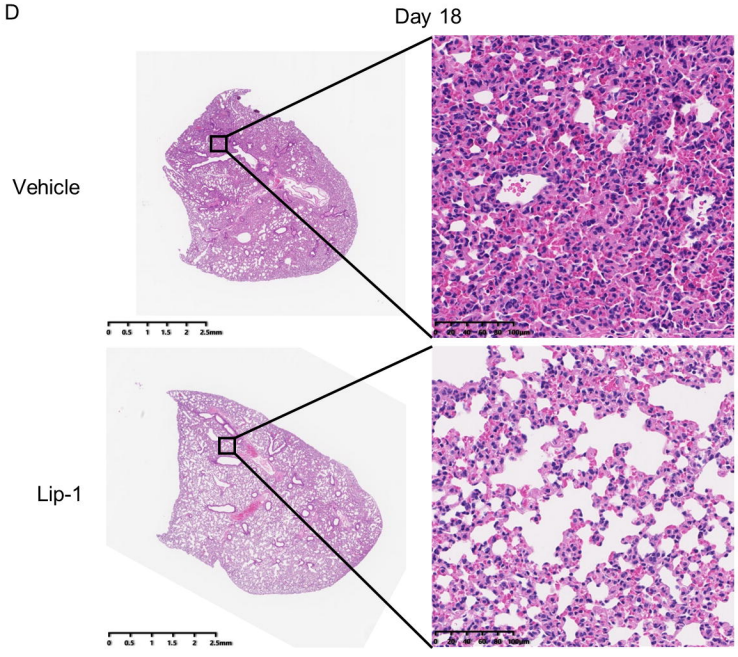
D
Day 18
Vehicle
Lip-1

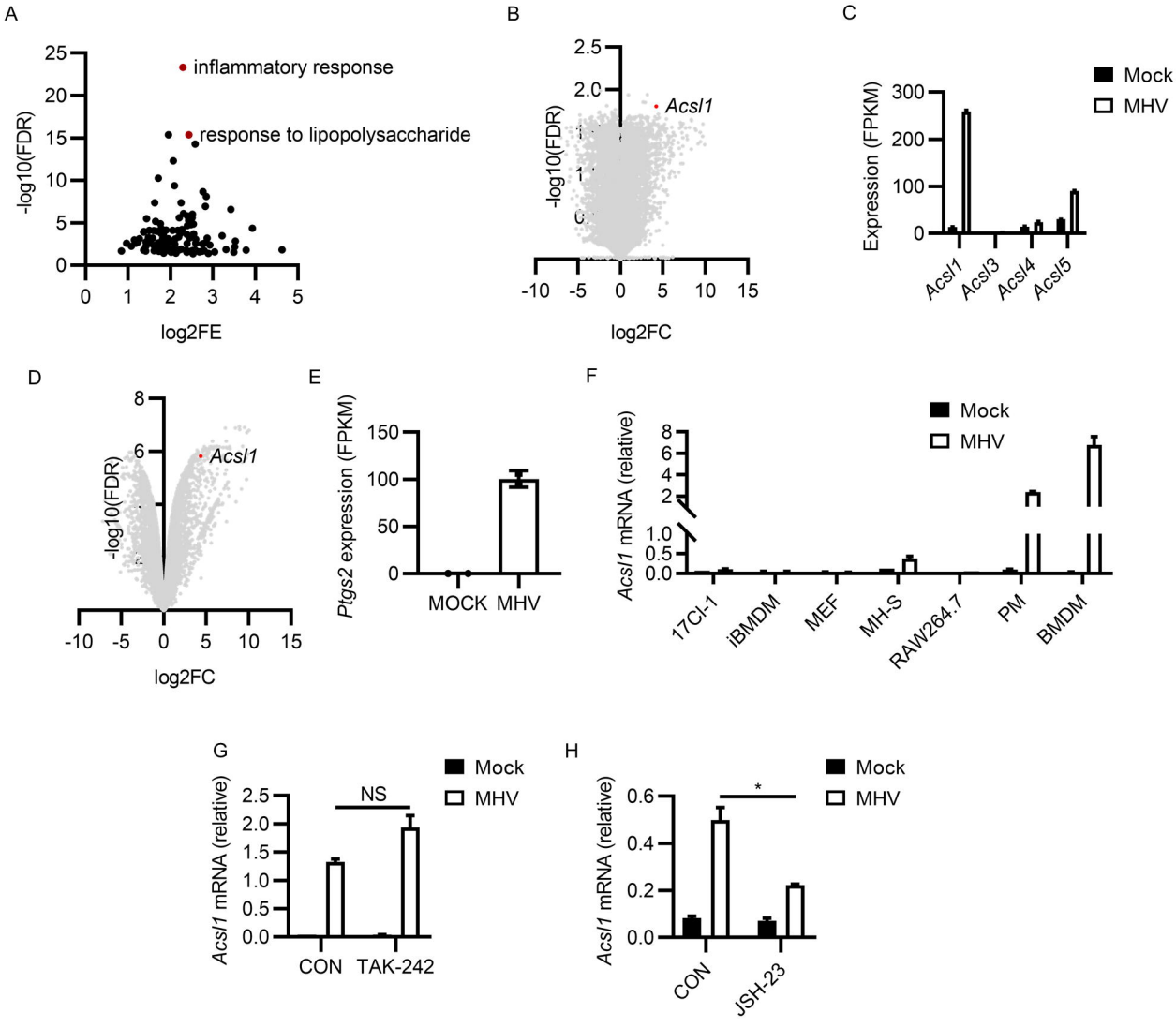
A
inflammatory response
response to lipopolysaccharide
-log10(FDR)
log2FE
B
Acsl1
-log10(FDR)
log2FC
C
Mock
MHV
Expression (FPKM)
Acsl1
Acsl3
Acsl4
Acsl5
D
Acsl1
-log10(FDR)
log2FC
E
Ptgs2 expression (FPKM)
MOCK
MHV
F
Mock
MHV
Acsl1 mRNA (relative)
17Cl-1
iBMDM
MEF
MH-S
RAW264.7
PM
BMDM
G
Mock
MHV
NS
Acsl1 mRNA (relative)
CON
TAK-242
H
Mock
MHV
*
Acsl1 mRNA (relative)
CON
JSH-23

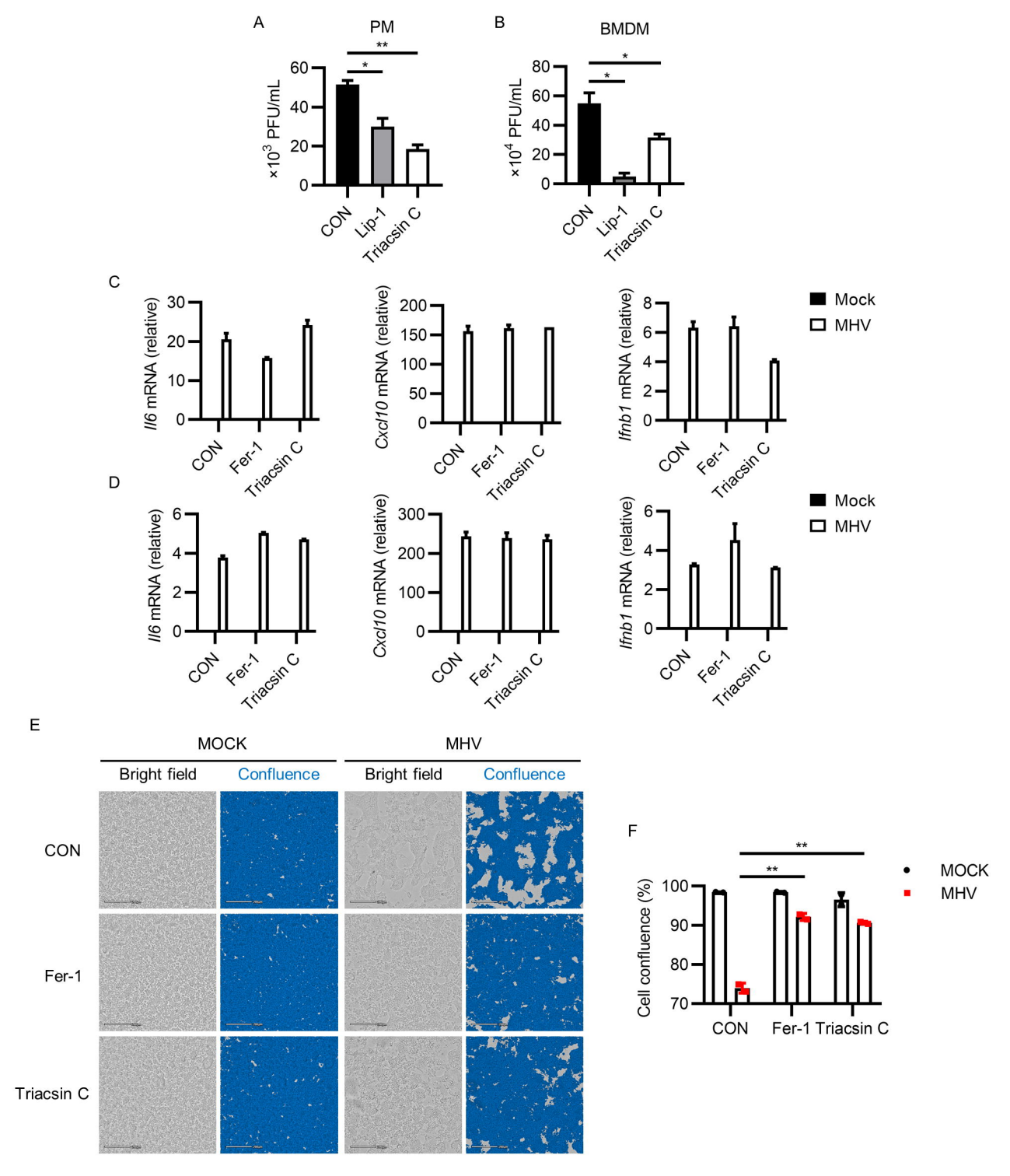
A
PM
**
*
60
40
20
0
×10^3 PFU/mL
CON
Lip-1
Triacsin C
B
BMDM
*
*
80
60
40
20
0
×10^4 PFU/mL
CON
Lip-1
Triacsin C
C
Il6 mRNA (relative)
30
20
10
0
CON
Fer-1
Triacsin C
Cxcl10 mRNA (relative)
200
150
100
50
0
CON
Fer-1
Triacsin C
Ifnb1 mRNA (relative)
8
6
4
2
0
CON
Fer-1
Triacsin C
Mock
MHV
D
Il6 mRNA (relative)
6
4
2
0
CON
Fer-1
Triacsin C
Cxcl10 mRNA (relative)
300
200
100
0
CON
Fer-1
Triacsin C
Ifnb1 mRNA (relative)
6
4
2
0
CON
Fer-1
Triacsin C
Mock
MHV
E
MOCK
MHV
Bright field
Confluence
Bright field
Confluence
CON
Fer-1
Triacsin C
F
**
**
Cell confluence (%)
100
90
80
70
CON
Fer-1
Triacsin C
MOCK
MHV